

## PAPER

[View Article Online](#)  
[View Journal](#) | [View Issue](#)Cite this: *J. Mater. Chem. A*, 2025, **13**, 10475Lattice variations in  $\text{CaTiO}_3$  cubes and cuboids and their use in photocatalytic benzimidazole formation†Ya-Ting Yang,<sup>a</sup> Bo-Hao Chen,<sup>ab</sup> Arnab Pal,<sup>c</sup> Chih-Hsueh Li,<sup>a</sup> Zong-Hong Lin<sup>c</sup> and Michael H. Huang<sup>id</sup>\*<sup>a</sup>

$\text{CaTiO}_3$  perovskite cubes with tunable sizes of 90 to 886 nm, as well as 156 and 725 nm cuboids, have been hydrothermally synthesized. Remarkably, despite their similar appearance, only cubes show a preferred orientation effect in X-ray diffraction (XRD) patterns. Peak positions also shift slightly with particle size and shape. Synchrotron XRD analysis reveals the presence of bulk and surface layer lattices with clearly shifted peaks. Unexpectedly, while a  $\text{CaTiO}_3$  cube presents (002) lattice fringes in transmission electron microscopy (TEM) images, a cuboid shows (001) lattice fringes. They also have discernably different lattice point patterns. These lattice features give rise to dissimilar dielectric constants and optical facet dependence. The cuboid crystals show stronger piezoelectric and ferroelectric responses than cubic particles do. Their surface properties differ completely with cuboidal particles being moderately active toward rhodamine B photodegradation, while cubes are inactive from floating above the dye solution with stirring. The  $\text{CaTiO}_3$  cuboids are more effective than cubes in photocatalyzing the formation of benzimidazole. This work demonstrates that interior lattice variations can significantly tune various materials properties, so detailed structural analysis is necessary to explain shape-related behaviors.

Received 20th January 2025  
Accepted 10th March 2025

DOI: 10.1039/d5ta00541h

[rsc.li/materials-a](https://rsc.li/materials-a)

## Introduction

Electrical conductivity, photocatalytic activity, and optical properties of semiconductor crystals have been found to depend on the exposed faces.<sup>1–9</sup> Moreover, magnetic and piezoelectric responses of oxide nanocrystals also exhibit facet dependence.<sup>10–13</sup> These phenomena have been found to originate from the presence of a surface layer region inside crystals with notable variations in lattice deviations, plus slight lattice constant changes in the interior bulk, as evidenced by synchrotron XRD patterns and fast Fourier transform (FFT)-processed high-resolution transmission electron microscopy (HR-TEM) images.<sup>9–11,14</sup> Because of the notably different lattice point variations in the surface layer region, charge carrier transport across a particular surface should encounter dissimilar energy barriers, and light with somewhat different wavelengths gets absorbed to tune the band gap. Since  $\text{SrTiO}_3$  crystals show large lattice constant changes and various facet-dependent behaviors, including use as a photocatalyst, it is

highly interesting to prepare other oxide perovskites such as calcium titanate to explore more facet-related behaviors and for use in photocatalysis.<sup>3,5,6,12,13</sup>  $\text{CaTiO}_3$ , with known band gaps in the range of 3.50–3.65 eV, has an orthorhombic crystal structure at room temperature, and can change to a tetragonal phase at 1498 K.<sup>15–17</sup> Some applications of  $\text{CaTiO}_3$  including photocatalytic dye degradation,  $\text{CO}_2$  reduction, and piezoelectric ceramics have been reported.<sup>18–20</sup> Previously,  $\text{CaTiO}_3$  cubes and square bars have been synthesized by forming a Ti-triethanolamine (TEOA) complex first.<sup>21</sup> A hydrogel-based growth of  $\text{CaTiO}_3$  rectangular blocks through the use of titanium isopropoxide and titanium *n*-butoxide in a basic solution environment is a common synthetic approach.<sup>15</sup> However, cuboids with sizes less than 500 nm have generally not been obtained. Hence, a research goal is to make much smaller  $\text{CaTiO}_3$  crystals for optical size effect demonstration and TEM characterization. Furthermore, it is desirable to produce  $\text{CaTiO}_3$  crystals with some interior lattice variations to observe changes in photocatalytic activity, piezoelectricity and ferroelectricity, as facet-dependent properties of  $\text{CaTiO}_3$  crystals have not been demonstrated.

In addition to typical photocatalytic dye degradation, the photogenerated electrons, holes, and radicals can be utilized to catalyze some organic oxidative reactions.<sup>22</sup> For example,  $\text{Cu}_2\text{O}$  polyhedral nanocrystals have been used to photocatalyze aryl-boronic acid hydroxylation, aryl sulfide oxidation, oxidative amine coupling, and aromatic thioamide cyclization

<sup>a</sup>Department of Chemistry, National Tsing Hua University, Hsinchu, 300044, Taiwan. E-mail: [hyhuang@mx.nthu.edu.tw](mailto:hyhuang@mx.nthu.edu.tw)<sup>b</sup>National Synchrotron Radiation Research Center, Hsinchu, 300092, Taiwan<sup>c</sup>Department of Biomedical Engineering, National Taiwan University, Taipei, 10617, Taiwan† Electronic supplementary information (ESI) available. See DOI: <https://doi.org/10.1039/d5ta00541h>

reactions.<sup>4,23–27</sup> Dimethylacrylamide photopolymerization can also be improved using Cu<sub>2</sub>O crystals.<sup>28</sup> Considering the higher structural stability of oxide perovskites than cuprous oxide, CaTiO<sub>3</sub> crystals should promote some organic reactions such as the formation of 2-aryl benzimidazoles.<sup>29</sup> 2-Aryl benzimidazoles are important structural motifs in agrochemicals and various pharmaceuticals.<sup>28–31</sup> Benzimidazoles have been synthesized by condensing *o*-phenylenediamine with aldehydes or alcohols, followed by oxidative cyclodehydrogenation. However, strong acidic/alkaline conditions and large amounts of oxidants may be required.<sup>32–36</sup> Pd-loaded TiO<sub>2</sub> nanospheres and ZnO nanosheets have also been employed for benzimidazole synthesis.<sup>37,38</sup> Alternatively, a hyper-crosslinked polymer was employed for the photocatalytic synthesis of benzimidazoles.<sup>39</sup> Photoirradiation on quinoline-bridged covalent organic frameworks also catalyzes benzimidazole formation.<sup>40</sup> These materials need elaborate synthesis steps and are costly, compared to using simple semiconductor crystals.

In this work, size-tunable CaTiO<sub>3</sub> cubes and cuboids have been synthesized for synchrotron XRD and TEM characterization. The interior lattice differences between cubes and cuboids suggest exposure of somewhat different crystal faces, supported by distinct variations in dye photodegradation, dielectric constant, and piezoelectric and ferroelectric responses. CaTiO<sub>3</sub> cuboids are more reactive than cubes toward photo-oxidative generation of benzimidazole, showing the benefit of interior lattice control to photocatalytic activity.

## Results and discussion

### Synthesis and structural characterization of CaTiO<sub>3</sub> cubes and cuboids

Large 695 and 886 nm CaTiO<sub>3</sub> cubes were synthesized in water, while 393 nm cubes and 725 nm cuboids were respectively

prepared in butanol and hexanol, by adopting synthetic conditions used to make SrTiO<sub>3</sub> and BaTiO<sub>3</sub> nanocrystals.<sup>5,12</sup> After mixing triethanolamine (TEOA) and TiCl<sub>4</sub> in a vial to form complex species, CaCl<sub>2</sub> and KOH solutions were added with stirring and transferred to an oven for crystal growth at 190–200 °C for 3 h. Fine adjustments in the concentration of reagents enable particle size and shape variation (Fig. S1 and Table S1, ESI†). Chloride ions have been introduced to give perovskite crystal shape control.<sup>41</sup> Addition of KCl in a water/ethanol solution was found effective to reducing the particle size (Table S2, ESI†). 90 and 212 nm CaTiO<sub>3</sub> nanocubes and 156 nm cuboids were synthesized. Varying the reagent concentration tunes the reaction quotient *Q* and the Gibbs free energy  $\Delta G$ . If  $\Delta H$  is similar in making different particle shapes,  $\Delta G$  should come from  $\Delta S$ , inferring that the interior lattice cannot be identical, and this yields the semiconductor facet and optical size effects. This analysis means that some lattice variations should naturally occur, particularly for particles exposing different surfaces.

Fig. 1 shows scanning electron microscopy (SEM) images of the synthesized 212 and 695 nm CaTiO<sub>3</sub> cubes and 156 and 725 nm cuboids. Table S3, ESI† gives their average dimensions along the three edges. SEM images of other-sized cubes are provided in Fig. S2, ESI†. Fig. S3, ESI† offers size distribution histograms of all the samples. Because of the orthorhombic nature of this material, the cube samples do not always contain perfect cubes; some elongated particles are also present. For the cuboid samples, the particles are mostly rectangular blocks. Other than this particle morphology difference, cubes and cuboids are primarily distinguished by differences in their XRD patterns and lattice plane images. Fig. 2 presents XRD patterns of CaTiO<sub>3</sub> cubes and cuboids. XRD patterns of size-tunable CaTiO<sub>3</sub> cubes are shown in Fig. S4, ESI†. All peaks match to the orthorhombic phase of CaTiO<sub>3</sub> without any impurity (space

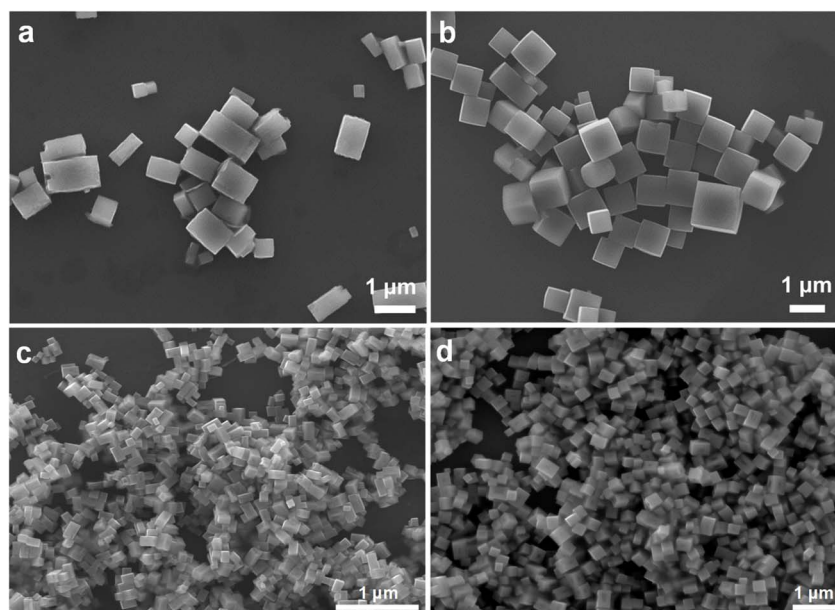


Fig. 1 SEM images of (a and c) 725 and 156 nm CaTiO<sub>3</sub> cuboids and (b and d) 695 and 212 nm CaTiO<sub>3</sub> cubes.



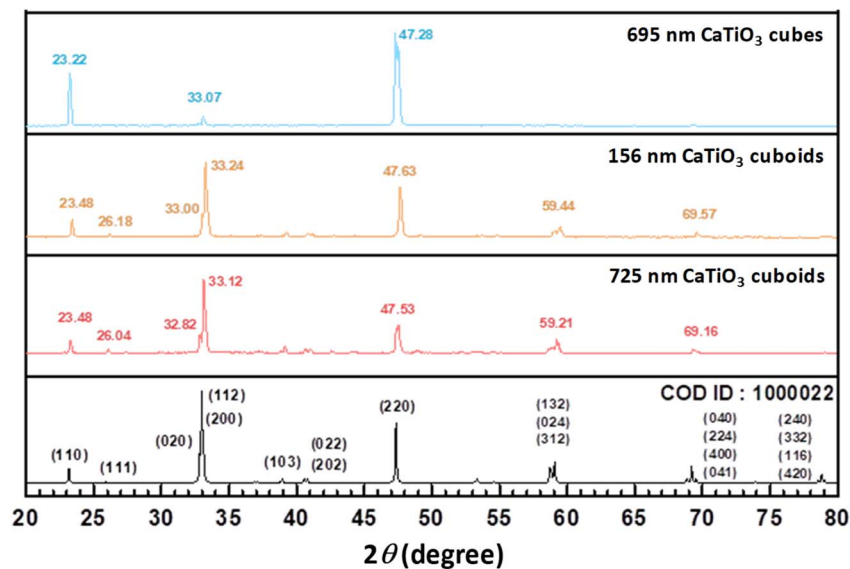


Fig. 2 XRD patterns of  $\text{CaTiO}_3$  cubes and cuboids and a reference XRD pattern.

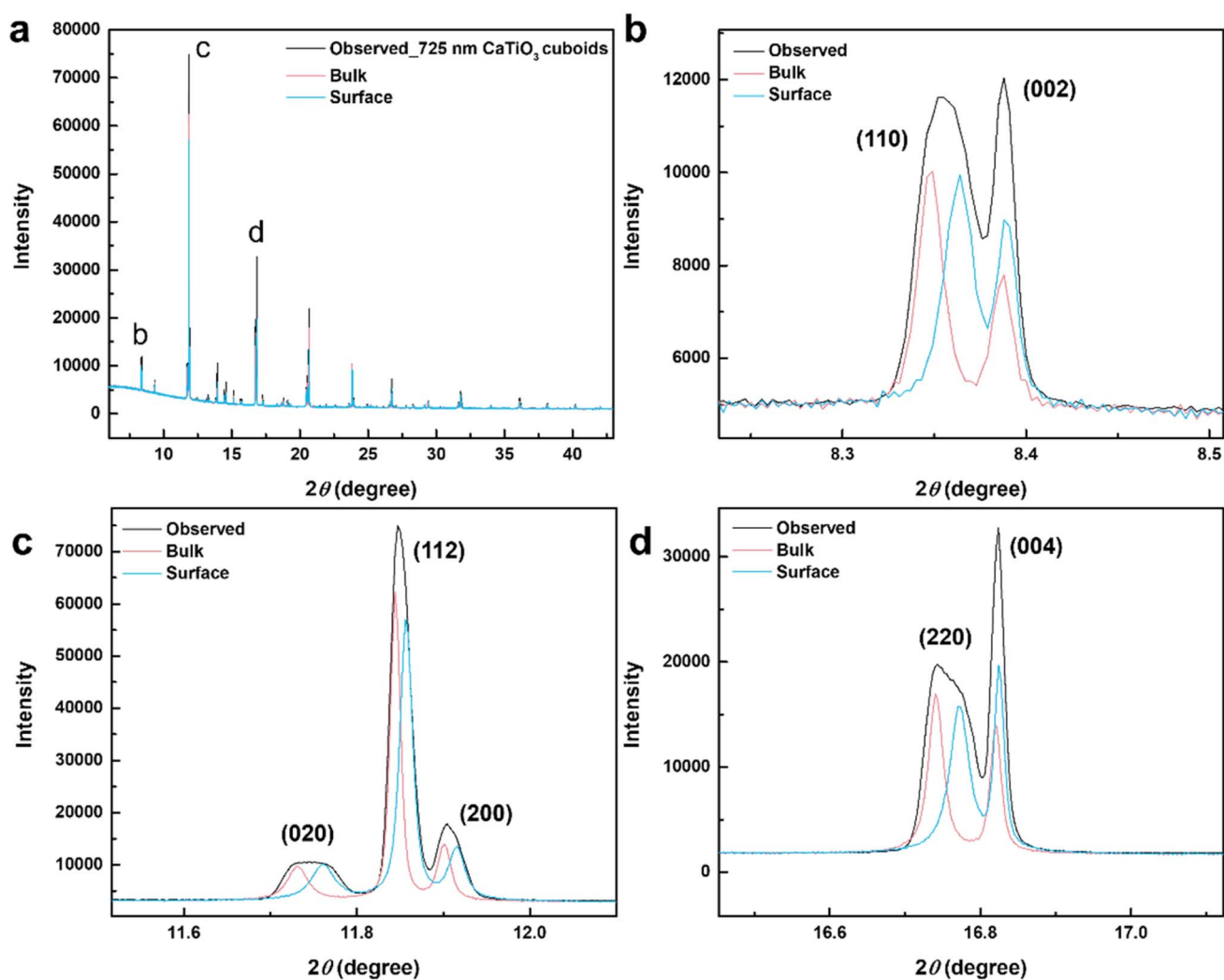


Fig. 3 (a) Rietveld refinement of XRD pattern of 725 nm  $\text{CaTiO}_3$  cuboids to yield bulk and surface layer lattices and (b–d) the expanded peaks.



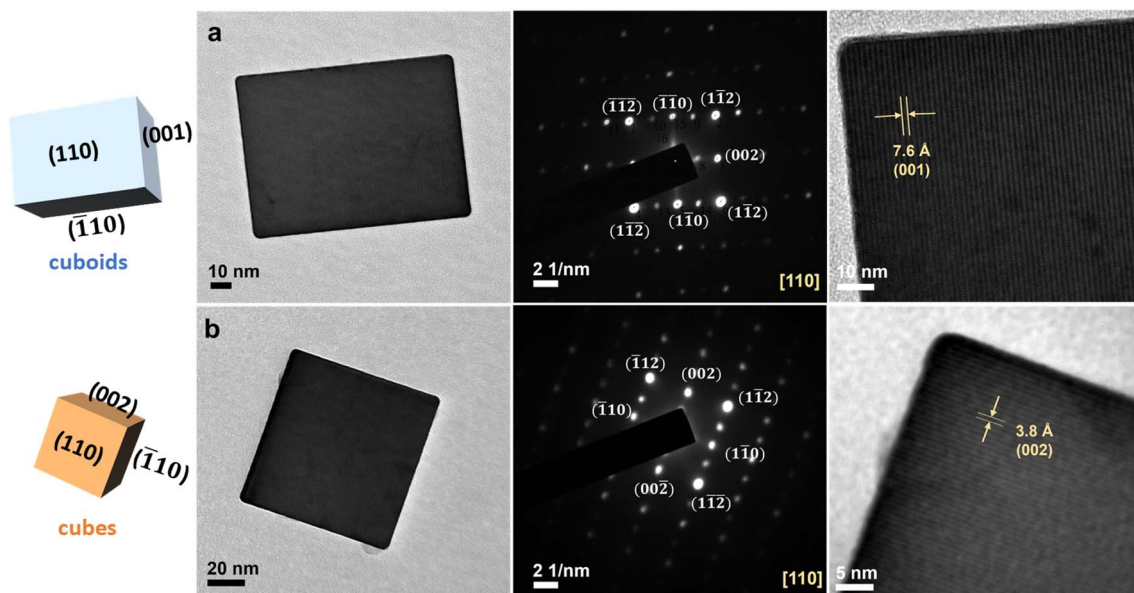


Fig. 4 TEM images, SAED patterns, and high-resolution TEM images of a single CaTiO<sub>3</sub> (a) cuboid and (b) cube. The exposed crystal faces are marked.

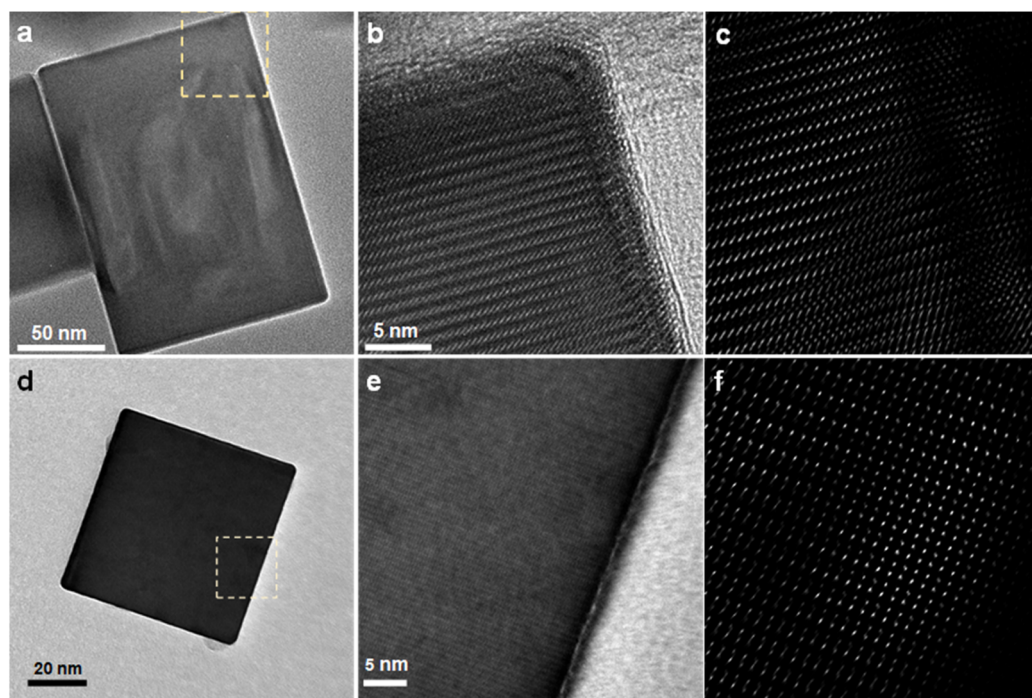


Fig. 5 High-magnification TEM images of (a) a CaTiO<sub>3</sub> cuboid and (d) a CaTiO<sub>3</sub> cube and (b and e) the expanded TEM images of the dashed regions. (c and f) FFT-processed lattice images of panels b and e.

group:  $P6mm$ ). Fig. S4, ESI† shows slight peak shifts to lower  $2\theta$  angles with increasing cube sizes, meaning the cell constants expand for larger cubes. Moreover, for all the cube samples, the (002)/(110) and (004)/(220) peaks have much stronger intensities than the (020)/(112)/(200) peaks, while all other peaks are not observed. This indicates that the exposed faces of cubes are

likely the {002} and {110} faces. By contrast, all the expected peaks are observed in the 156 and 725 nm cuboid samples. The (112)/(200) peak has the highest intensity, resembling that of the reference diffraction pattern. The results suggest that the exposed crystal faces for cuboids may be different. Further structural characterization is needed.



An important aspect of XRD analysis is to observe the presence of bulk and surface layer lattices from splitting or deconvolution of diffraction peaks. The surface layer lattice likely originates from temperature-induced lattice deviations, and the crystal surfaces are most affected by the reaction temperature. Heating crystals resembles barbecuing steak, but the temperature effect is often not considered when explaining crystal properties. High-resolution diffraction signals were collected at the TPS19A beamline of the Taiwan photon source.  $\text{CaTiO}_3$  powder was packed into a 0.2 mm diameter capillary tube. Data were collected using X-ray radiation with a wavelength of 0.56025 Å (X-ray energy of 28.56 keV) under a 30 second exposure condition. The peak positions have been adjusted for a  $2\theta$  zero-point shift. Close examination reveals the peaks are broadened or appear asymmetric, especially for the (110) and (220) peaks. To address the issue of peak asymmetry, a multi-phase Rietveld refinement incorporating a generalized micro-strain model was employed to improve fitting of the diffraction patterns. This refinement approach allows for the resolution of two lattice components for both cuboids and cubes, representing bulk and surface layer lattices. Fig. 3 and S5, ESI† display Rietveld refinement results of the synchrotron XRD patterns for 725 nm  $\text{CaTiO}_3$  cuboids and 695 nm cubes. Table S4, ESI† summarizes the refinement results. The bulk and surface phases are determined based on the magnitude of the mean microstrain value. Typically, a higher microstrain value is assigned to the surface phase, whereas a lower value is designated to the interior bulk. For cubes, the surface phase accounts for 27.7% by weight. Remarkably, the surface phase represents 54.0% by weight for cuboids. The presence of bulk and surface layer lattices should be broadly observable in ionic solids, as thermal lattice stress during crystal growth cannot be fully relaxed when the particles are returned to room temperature.

TEM characterization was found important to the assignment of the faces of  $\text{CaTiO}_3$  cubes and cuboids. As seen in Fig. 4, the selected-area electron diffraction (SAED) patterns, recorded along the [110] zone axis, give discrete spots, confirming the single-crystalline nature of these particles. Please note that the small spots are only observed along the  $c$ -axis for both samples, showing the six crystal faces are not all equivalent even for the cube. The viewing zone axis and the diffraction spots are assigned following a report on  $\text{CaTiO}_3$ .<sup>42</sup> The HR-TEM images reveal lattice fringes. The (002) planes of the cube are perpendicular to the (002) spot direction with a  $d$ -spacing of 3.8 Å. The cuboid presents lattice fringes along the  $c$ -axis measuring 7.6 Å, and are assigned (001) planes. The fact lattice fringe distance of the cuboid is twice that of the cube indicates that these two samples are not identical, despite having the same SAED pattern. On the basis of TEM and XRD results, it is concluded that both shapes expose equivalent  $\{110\}/\{\bar{1}10\}$  faces, with the cuboid and cube exposing  $\{001\}$  and  $\{002\}$  faces, respectively. This assignment also takes into account that their various properties are not the same, so there must be intrinsic lattice differences to understand such behaviors.

Fig. 5 shows again that the fringe spacings and lattice features look strikingly different between a cube and a cuboid, with fringes more widely separated for the cuboid. The lattice

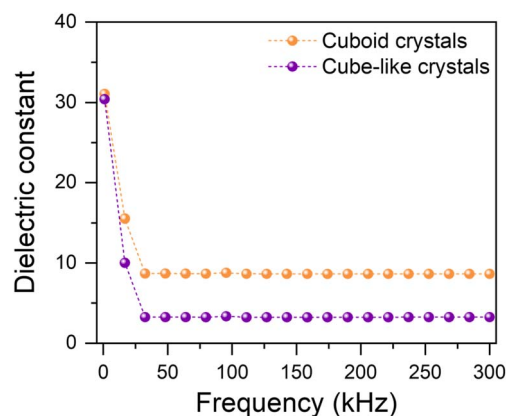


Fig. 6 Frequency-dependent dielectric constants of small-sized  $\text{CaTiO}_3$  cubes and cuboids.

deviations can be directly observed by FFT processing of the collected HR-TEM images. For the cuboid (Fig. 5c), the spots appear to align diagonally to the crystal edges, and become more stretched in the interior region. By contrast, the cube shows less spot deviations, yet strangely the adjacent spots point in alternate directions. Similar criss-cross lattice pattern has been observed in  $\{111\}$ -exposing  $\text{Cu}_2\text{O}$  crystals.<sup>14</sup> These lattice spot patterns further suggest that the interior lattices are distinctly different for the  $\text{CaTiO}_3$  cubes and cuboids, which should reflect in their properties. As a way to probe the interior lattice, dielectric constant measurements on  $\text{CaTiO}_3$  cubes and cuboids were performed (see Fig. 6). The cuboids consistently have higher dielectric constants across the measured frequency range (0–300 kHz). The appreciable dielectric constant differences between the two samples illustrate again that interior lattice variations can significantly affect the crystal properties.

X-ray photoelectron spectroscopy (XPS) was utilized to check the chemical state of the  $\text{CaTiO}_3$  crystals. The complete XPS data for 725 nm  $\text{CaTiO}_3$  cuboids are shown in Fig. S6, ESI†. The Ca  $2p_{3/2}$  and Ca  $2p_{1/2}$  peaks are centered at 346.5 eV and 350.1 eV, respectively. The Ti  $2p_{3/2}$  and  $2p_{1/2}$  peaks are respectively located at 458.4 eV and 464.2 eV. The major O 1s peak at 529.8 eV comes from  $\text{CaTiO}_3$ , while the minor peak at 531.3 eV is attributed to chemisorbed oxygen resulting from surface hydroxyl (OH) groups. These binding energies closely align with the reported XPS data of  $\text{CaTiO}_3$ .<sup>43</sup>

### Optical, piezoelectric, and ferroelectric property characterization

Fig. S7, ESI† presents diffuse reflectance spectra of the size-tunable  $\text{CaTiO}_3$  cubes, acquired using an integrating sphere. The converted Tauc plot gives their band gaps. Band gaps for 90, 253, 393, and 886 nm cubes are 3.61, 3.58, 3.49, and 3.46 eV, respectively. With increasing particle sizes, band gap continues to decrease even with large crystals. This is the general observation for semiconductor crystals. This happens partly because of the slight lattice constant changes with particle size. Fig. 7 shows the similarly-sized 695 nm  $\text{CaTiO}_3$  cubes and 725 nm cuboids have band gaps of 3.49 and 3.41 eV, respectively. The band gap difference still exists for these large crystals,



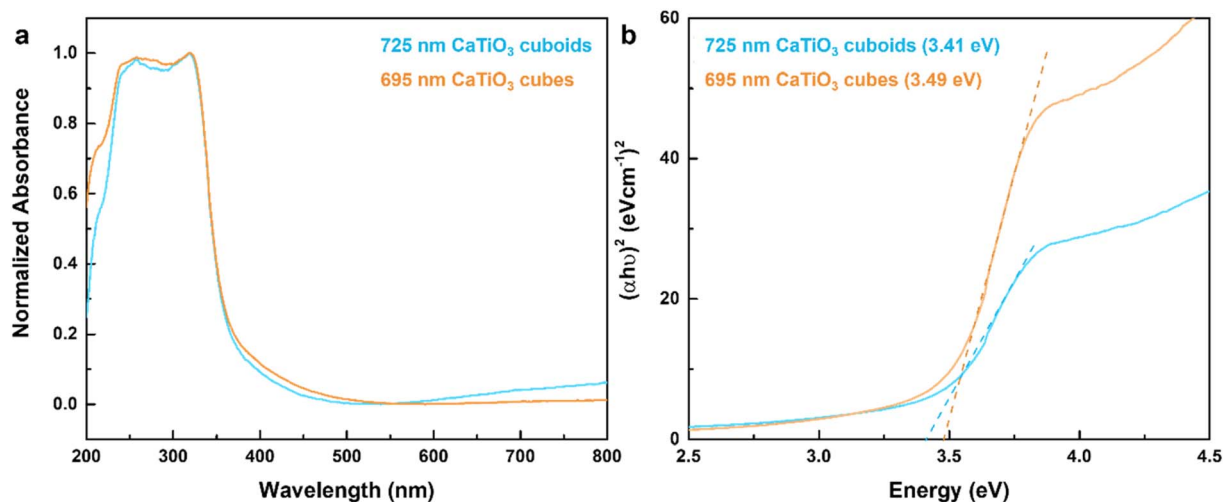


Fig. 7 (a) Diffuse reflectance spectra of  $\text{CaTiO}_3$  cubes and cuboids and (b) the corresponding Tauc plot.

suggesting that the internal lattice variations result in such an optical effect.

Since  $\text{CaTiO}_3$  has the same crystal structure as  $\text{BaTiO}_3$ , the synthesized particles were examined for possession of piezoelectricity and ferroelectricity properties. Piezoelectric force microscopy (PFM) measurements reveal that the cuboid generates a notably higher voltage than that of the cube, indicating the effect of internal lattice variations to piezoelectricity (Fig. 8).<sup>44</sup> The phase-voltage hysteresis

measurements show a ferroelectric switching behavior with a sharp phase transition around 0 V bias. A cuboid gives a larger hysteresis loop, further validating the interior lattice effect on ferroelectric response.

#### Photocatalytic dye photodegradation and benzimidazole formation

The surface facet difference between  $\text{CaTiO}_3$  cubes and cuboids is also manifested in their response to photodegradation of

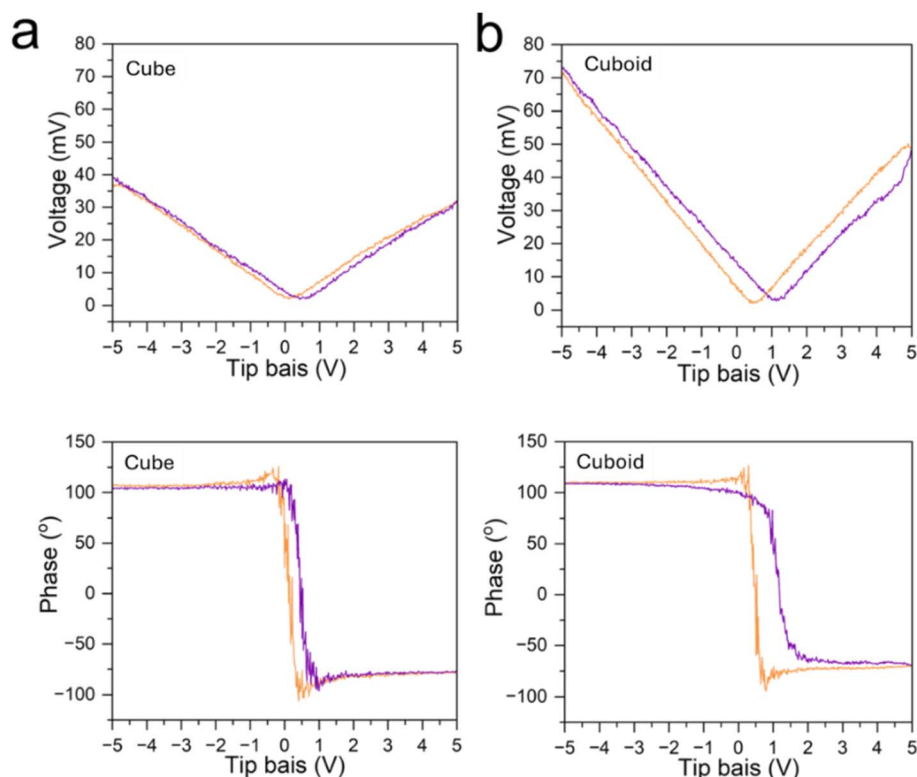


Fig. 8 Piezoelectric and ferroelectric characterization of a single  $\text{CaTiO}_3$  (a) cube and (b) cuboid. The voltage-amplitude butterfly loops (top panels) reveal the piezoelectric response under applied tip bias from  $-5$  V to  $+5$  V, and the corresponding phase-voltage hysteresis loops demonstrate their ferroelectric switching behavior.



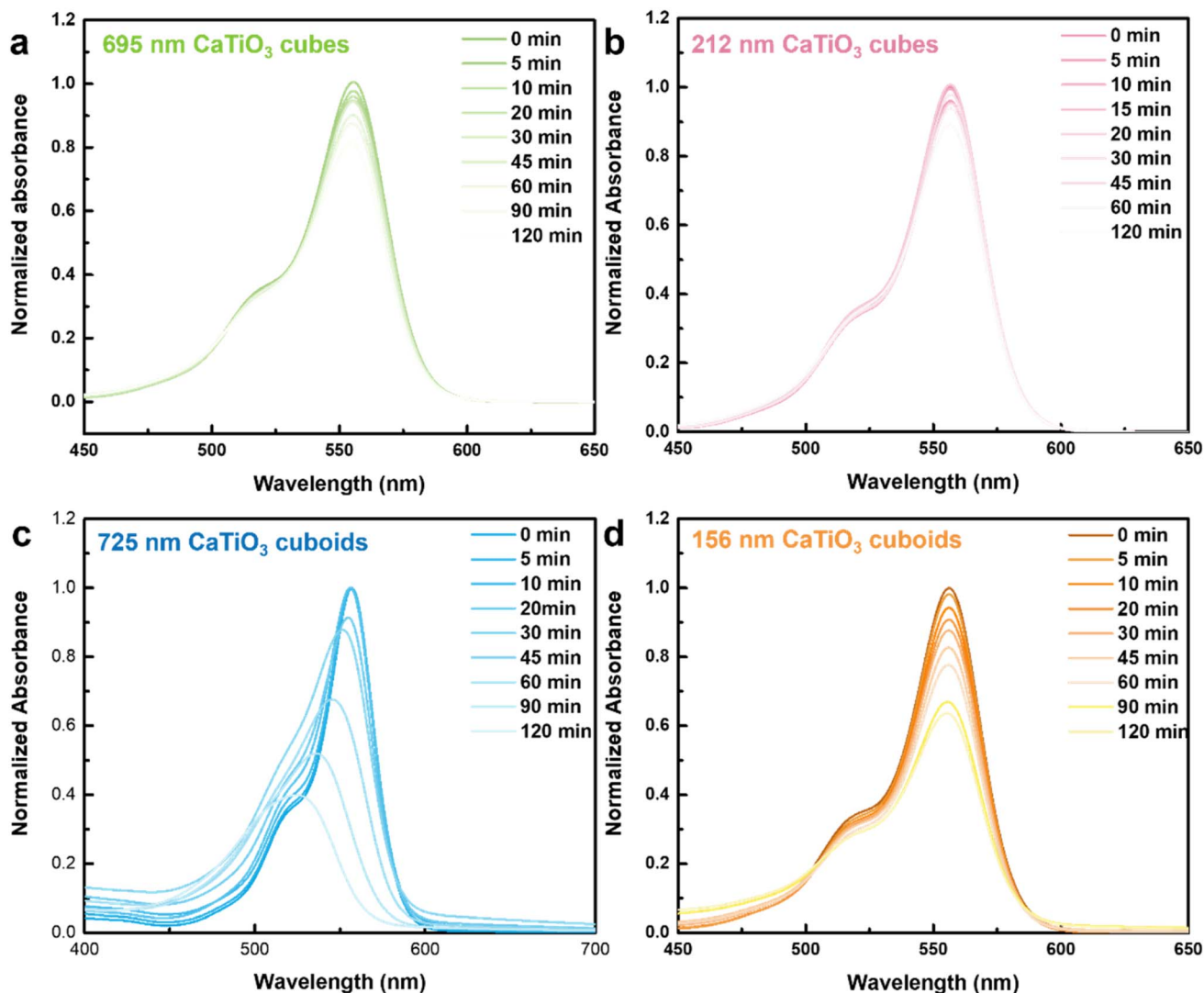
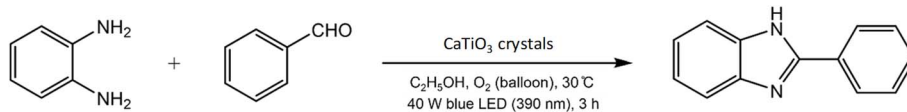


Fig. 9 Time-dependent UV-vis absorption spectra of rhodamine B photodegraded by (a) 695 nm cubes, (b) 212 nm cubes, (c) 725 nm cuboids, and (d) 156 nm cuboids.

Table 1  $\text{CaTiO}_3$ -photocatalyzed formation of benzimidazole<sup>a</sup>



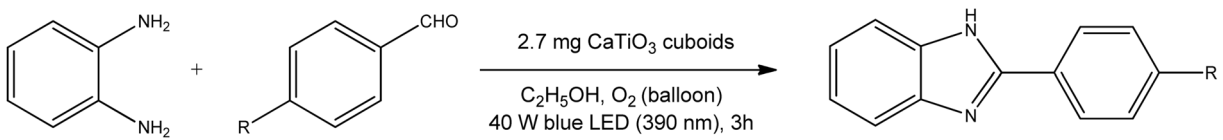
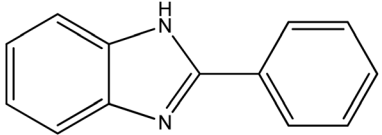
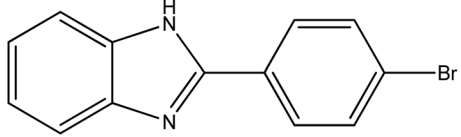
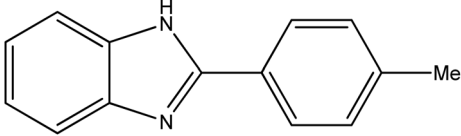
Entry	Crystals	Amount (mg)	Yield (%)
1	725 nm cuboids	2.7	99
2	156 nm cuboids	2.7	94
3	212 nm cubes	2.7	83
4	695 nm cubes	3.5	66
5	No catalyst	0	60

<sup>a</sup> Reagents: *o*-phenylenediamine (0.2 mmol), benzaldehyde (0.2 mmol), and ethanol (3 mL). Triphenylmethane was used as the internal standard.





Table 2 Substrate scope for CaTiO<sub>3</sub>-photocatalyzed formation of benzimidazoles<sup>a</sup>

		
Entry	Formula	Yields (%)
1		99
2		84
3		67

<sup>a</sup> Reagents: *o*-phenylenediamine (0.2 mmol), CaTiO<sub>3</sub> cuboids (2.7 mg), and ethanol (3 mL). Triphenylmethane was used as the internal standard.

rhodamine B. The band positions of CaTiO<sub>3</sub> is well situated to photogenerate hydroxyl radicals ( $\cdot\text{OH}$ ) and superoxide anion radicals ( $\text{O}_2^{\cdot-}$ ) for dye degradation.<sup>15</sup> For fair comparison, the total surface area of different samples was fixed (Table S3, ESI†). Fig. 9 presents time-dependent UV-vis absorption spectra of rhodamine B photodegraded by various CaTiO<sub>3</sub> crystals in a pH 4 solution. An acidic solution has been found to enhance photocatalytic activity.<sup>45</sup> Cuboids are apparently much more photocatalytically active than cubes. Interestingly, while 156 nm cuboids show a slowly decreasing absorption band at 556 nm, 725 nm cuboids display a progressive blue-shifted absorption band to 525 nm after 2 h. This is due to continuous de-ethylation of rhodamine B.<sup>46</sup> The cuboid morphology can be preserved after the reaction (Fig. S8, ESI†). By contrast, CaTiO<sub>3</sub> cubes were practically inactive toward rhodamine B degradation; the slight absorbance drop may be attributed to molecular adsorption on the particles. After some stirring, the cubes were found to become floated to the solution surface possibly from some electrostatic repulsion with the {002} faces of cubes, so light could not reach the particles. A similar behavior has been observed in Cu<sub>2</sub>O crystals.<sup>47,48</sup> Thus, exposure of some different surfaces can have profound effect on surface and photocatalytic properties.

The photogenerated charge carriers and radicals can be utilized to catalyze some organic reactions producing higher-value chemicals. We consider the coupling reaction between *o*-phenylenediamine and benzaldehyde to form benzimidazole.

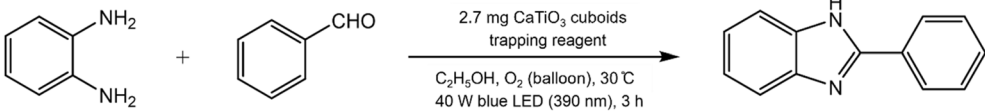
Fig. S9, ESI† illustrates the procedure for the synthesis of benzimidazoles with air purged. An oxygen balloon was employed. In the absence of any CaTiO<sub>3</sub> crystals, the reaction still occurred in ethanol at room temperature (30 °C from 390 nm light irradiation with fan cooling) with a 60% product yield in 3 h (Table 1). The use of 156 and 725 nm CaTiO<sub>3</sub> cuboids to photocatalysis this reaction delivered exceptional 94% and 99% product yields in 3 h, respectively. Using the same amount of 212 nm cubes gave a product yield of 83%. Adding 3.5 mg of 695 nm cubes, having the same particle surface area as that of 2.7 mg of 725 nm cuboids, produced a yield of just 66%. Apparently, the cuboids are more effective for this reaction. SEM image indicates retention of cuboid particle morphology after the reaction (Fig. S10, ESI†). Moreover, 2.7 mg of micron-sized CaTiO<sub>3</sub> cubes were employed for three cycles of the photocatalytic benzimidazole synthesis (Fig. S11, ESI†). Product yields of 67, 63 and 62% were obtained, demonstrating the recyclability of the photocatalyst. Subsequently, benzaldehydes with bromo and methyl group substituents were introduced for the reaction using 725 nm cuboids as the photocatalyst (Table 2). The 2-(4-bromophenyl)-benzimidazole yield was 84%, while 2-(4-methylphenyl)-1H-benzimidazole yield was 67%. These results demonstrate that CaTiO<sub>3</sub> crystals can be used to synthesize different benzimidazoles.

To propose a reaction mechanism, electron, hole and radical trapping experiments were performed using 725 nm cuboids (Table 3). In the presence of KBrO<sub>3</sub>, acting as an electron

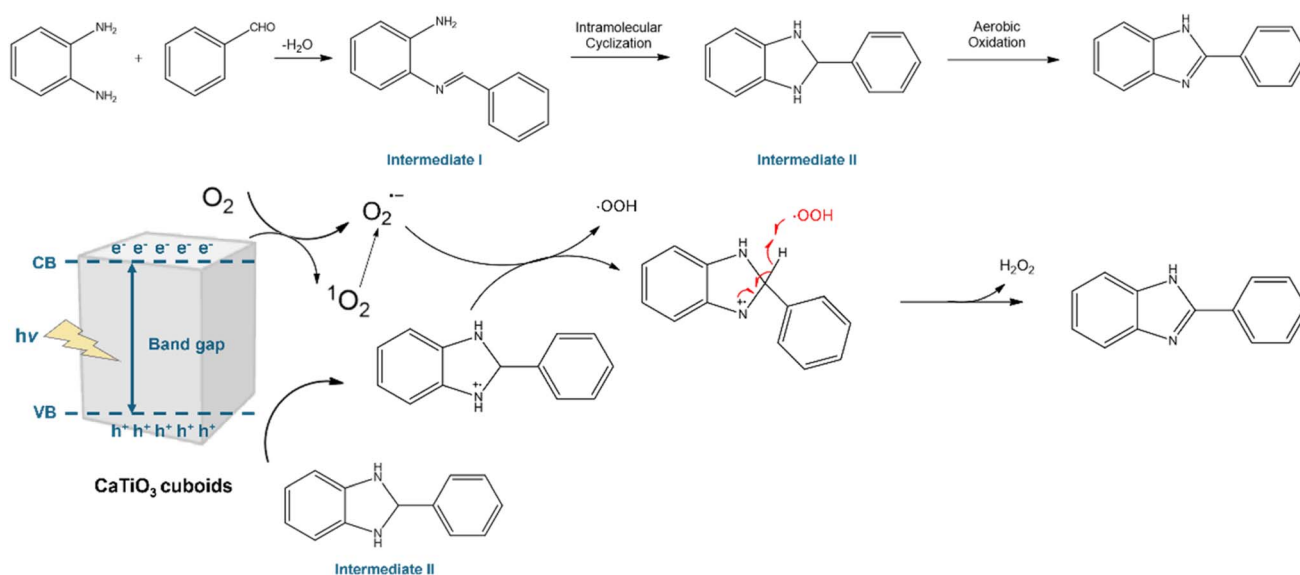




Table 3 Reactive oxygen species and hole trapping experiments<sup>a</sup>

		
Entry	Trapping reagent	Yields (%)
1	KBrO <sub>3</sub>	68
2	DIPEA	20
3	<i>tert</i> -Butanol	82
4	DABCO	27
5	1,4-Benzoquinone	57.5

<sup>a</sup> Reagents: *o*-phenylenediamine (0.2 mmol), benzaldehyde (0.2 mmol), and ethanol (3 mL). Triphenylmethane was used as the internal standard. DIPEA = *N,N*-diisopropylethylamine. DABCO = 1,4-diazabicyclo [2,2,2]octane.

Fig. 10 Proposed reaction mechanism of CaTiO<sub>3</sub>-photocatalyzed formation of benzimidazoles.

scavenger in the reaction, product formation dropped from 99% to just 68%. The photoexcited electrons should migrate to the crystal surface and react with oxygen to form superoxide anion radicals. *N,N*-Diisopropylethylamine (DIPEA), introduced as a hole scavenger, greatly inhibited the reaction to a yield of only 20%. Hole transfer should take part in the reaction mechanism. Next, *tert*-butanol, a common hydroxyl radical scavenger, was added into the reaction. A relatively small decrease in yield was observed, so  $\cdot\text{OH}$  radicals are less important for this reaction. The yield dropped sharply to 27% upon adding 1,4-diazabicyclo [2,2,2]octane (DABCO), suggesting the involvement of singlet oxygen in the formation of benzimidazoles. Singlet oxygen may gain an electron to form a superoxide anion radical. Removal of singlet oxygen can mean less superoxide radicals are available. Finally, addition of 1,4-benzoquinone as a superoxide anion radical scavenger resulted in 57.5% yield. Superoxide radicals are involved in the photocatalytic reaction.

Electron paramagnetic resonance (EPR) measurement was performed to further establish the involved radicals. Due to the short lifetime of free radicals, we employed a spin-trapping reagent DMPO to stabilize them. DMPO captures superoxide radicals, forming a DMPO-OOH adduct that displays a 12-line EPR spectrum. This adduct is highly unstable and rapidly degrades into the DMPO-OH adduct, which gives a 4-line EPR spectrum with a relative intensity ratio of 1 : 2 : 2 : 1.<sup>49</sup> Fig. S12, ESI† is the EPR spectrum obtained in methanol to prolong the adduct lifetime. The signal corresponds to DMPO-OOH adducts, indicating that mainly superoxide radicals are generated.

From the trapping experiments and EPR result, two pathways for the formation of benzimidazole are proposed (Fig. 10). In the absence of any photocatalyst, *o*-phenylenediamine and benzaldehyde first condense to form an imine (intermediate I).<sup>50</sup> Intramolecular cyclization takes place to produce intermediate II, which undergoes aerobic oxidation to yield a benzimidazole. The



second pathway involves  $\text{CaTiO}_3$  nanocrystals under light irradiation to generate electron–hole pairs. Holes primarily facilitate the oxidation of intermediate II into the corresponding cationic radicals. Simultaneously, the photoexcited electrons would reduce oxygen to form superoxide radicals. Singlet oxygen may gain an electron to form a superoxide anion radical. Upon deprotonation of intermediate II by  $\text{O}_2^{\cdot-}$  and subsequent dehydrogenation using the hydroperoxyl radical  $\text{HOO}^\cdot$ , benzimidazole is produced along with the formation of hydrogen peroxide.<sup>39,40</sup>

## Conclusions

Size-tunable  $\text{CaTiO}_3$  perovskite cubes and cuboids have been hydrothermally synthesized. Despite they have the same crystal structure, all the cube samples show particularly strong (002)/(110) set of peaks in their XRD patterns. Synchrotron XRD analysis also reveals distinct bulk and surface layer lattices for cubes and cuboids. Interestingly, while (002) planes are observed in the TEM images of a cube, a cuboid only exhibits (001) planes, suggesting exposure of different crystal surfaces for cubes and cuboids. Their lattice point patterns also differ considerably. These lattice variations can explain their optical facet effect and changes in dielectric constant. A cuboid generally shows stronger piezoelectric and ferroelectric responses than a cube does. The different surface properties of cubes and cuboids have been demonstrated in the photo-degradation of rhodamine B with active cuboids and inactive/floating cubes. Cuboids are more effective than cubes toward photocatalytic formation of benzimidazole from coupling of *o*-phenylenediamine and benzaldehyde. This work shows that significant interior lattice variations can exist in semiconductor particles with the same crystal structure. The lattice variations greatly influence their various properties and can be capitalized for enhanced performance.

## Experimental

### Chemicals

Titanium tetrachloride ( $\text{TiCl}_4$ , 99%, Acros Organics), calcium chloride dihydrate ( $\text{CaCl}_2 \cdot 2\text{H}_2\text{O}$ , 99+%, Honeywell), calcium nitrate tetrahydrate ( $\text{Ca}(\text{NO}_3)_2 \cdot 4\text{H}_2\text{O}$ , 99+%, Alfa Aesar), potassium hydroxide (KOH, 85%, Honeywell), ethanol ( $\text{C}_2\text{H}_5\text{OH}$ , 99.8%), potassium chloride (KCl, 99%, SHOWA), triethanolamine ( $\text{C}_6\text{H}_{15}\text{NO}_3$ , >99%, Sigma), nitric acid ( $\text{HNO}_3$ , 70%, Acros Organics), *o*-phenylenediamine ( $\text{C}_6\text{H}_8\text{N}_2$ , 98%, Thermo Scientific), benzaldehyde ( $\text{C}_6\text{H}_5\text{CHO}$ , 98%, Sigma), triphenylmethane ( $(\text{C}_6\text{H}_5)_3\text{CH}$ , 98%, NOVA), methanol ( $\text{CH}_3\text{OH}$ , 99.8%, Honeywell), *tert*-butanol ( $\text{C}_4\text{H}_{10}\text{O}$ , >99%, Sigma-Aldrich), DABCO ( $\text{C}_6\text{H}_{12}\text{N}_2$ , 98%, Alfa Aesar), DMPO ( $\text{C}_6\text{H}_{11}\text{NO}$ , 98%, Matrix Scientific), 1,4-benzoquinone ( $\text{C}_6\text{H}_4\text{O}_2$ , 98%, Alfa Aesar), *N,N*-diisopropylethylamine ( $\text{C}_8\text{H}_{19}\text{N}$ , 99.5%, Acros Organics), and potassium bromate ( $\text{KBrO}_3$ , 99%, Alfa Aesar) were used as received.

### Synthesis of $\text{CaTiO}_3$ cubes and cuboids

The reagent amounts used and procedure for growing 393, 695 and 886 nm  $\text{CaTiO}_3$  cubes and 725 nm  $\text{CaTiO}_3$  cuboids are

shown in Table S1 and Fig. S1, ESI†. The reagent amounts and reaction time and temperature were carefully adjusted, including the use of butanol and hexanol for growing 383 nm  $\text{CaTiO}_3$  cubes and 735 nm cuboids. Using the formation of 886 nm cubes as an example, 15.7 mL of 2.0 M triethanolamine solution and 4.033 mL of water were added to a vial. The mixed solution was stirred for 5 min, and 0.041 mL of  $\text{TiCl}_4$  solution was added slowly under vigorous stirring for 5 min. Next, 0.314 mL of 1.187 M  $\text{CaCl}_2 \cdot 2\text{H}_2\text{O}$  solution was introduced and stirred for 30 min, followed by dropwise addition of 0.5 mL of 5 M aqueous KOH solution with stirring for 1 min. The solution was transferred to a 25 mL Teflon autoclave and heated at 200 °C in an oven for 3 h. After cooling to ambient temperature, the precipitate was recovered by centrifugation and washed several times with 2 M  $\text{HNO}_3$  solution, distilled water, and ethanol. Table S2, ESI† provides the reagent amounts used to make 212 and 90 nm  $\text{CaTiO}_3$  cubes and 156 nm  $\text{CaTiO}_3$  cuboids. Procedure for making these smaller particles are also available in the ESI.†

### Piezoelectric and ferroelectric measurements

These measurements were carried out *via* piezoelectric force microscopy using a ScanAsyst-enabled Bruker dimension icon atomic force microscope with a Pt/Ir-coated silicon cantilever (OSCM-PIT) as the conductive probe.<sup>51</sup> The high-speed pulse repetition drive frequency for the piezo response measurements was set at 189 kHz. An externally applied tip bias of 200 mV was used to enhance the piezo-response difference among different crystal shapes. All the measurements were done in ambient conditions.

### Photocatalytic synthesis of benzimidazole using $\text{CaTiO}_3$ cuboids

In this experiment, *o*-phenylenediamine (0.2 mmol) and  $\text{CaTiO}_3$  cuboids weighing 2.7 mg were placed in a 15 mL oven-dried quartz tube along with a stir bar, and the tube was sealed with a rubber septum (Fig. S2, ESI†). The tube was evacuated using a vacuum pump and refilled with oxygen three times using an oxygen balloon, then 3 mL of ethanol containing 0.2 mmol of benzaldehyde was introduced into the tube. The mixture underwent sonication for 1 min, followed by exposure to light from a 40 W LED ( $\lambda = 390$  nm). The light power density reaching the sample has been measured to be  $0.51 \text{ W cm}^{-2}$ . The reaction mixture was stirred for 3 h at room temperature. After the reaction, the solution underwent centrifugation at 11 000 rpm for 2.5 min to facilitate separation. The supernatant was collected with care and concentrated using a rotary evaporator under vacuum.

### Instrumentation

A thermal field emission scanning electron microscope (JEOL JSM-7000F) was used to check particle morphology. A D2 Phaser powder X-ray diffractometer with Cu K $\alpha$  radiation was used to identify the crystalline structure of  $\text{CaTiO}_3$  powder. Synchrotron XRD data were collected at the Taiwan Photon Source 19A beamline (TPS19A). The hard X-ray source was



delivered from an in-vacuum cryogenic undulator (CU15), and the powder diffraction patterns were recorded using a position-sensitive detector MYTHEN 18 K. Surface analysis was performed using a high-resolution X-ray photoelectron spectrometer (HR-XPS, PHI QuanteraII). TEM characterization was conducted on a JEOL JEM-F200 electron microscope. UV-vis absorption spectra were collected using a JASCO V-670 spectrometer with a solid sample holder attached. The dielectric constant measurements were performed using a GW Instek LCR-6300 high-precision meter. A Bruker ELEXSYSE 580 CW/Pulse spectrometer was used to obtain EPR spectra.  $^1\text{H}$  NMR spectra were obtained with the use of a Bruker Avance II 400 MHz NMR spectrometer. Chemical shifts ( $\delta$ ) are reported in ppm with the residual solvent signal as internal standard ( $d$ -DMSO at 2.5 ppm for  $^1\text{H}$  NMR).

## Data availability

All the data have been presented in the manuscript and ESI.†

## Conflicts of interest

There are no conflicts to declare.

## Acknowledgements

Financial support is provided by the National Science and Technology Council of Taiwan (NSTC 112-2113-M-007-016-MY3 and 113-2628-E-002-010-MY3). Ms. Swee-Lan Cheah of the NTHU Instrumentation Center assisted in the XPS analysis.

## References

- 1 A.-T. Lee, C.-S. Tan and M. H. Huang, *ACS Cent. Sci.*, 2021, **7**, 1929–1937.
- 2 G. Kumar, C.-R. Chen, B.-H. Chen, J.-W. Chen and M. H. Huang, *J. Mater. Chem. C*, 2022, **10**, 12125–12131.
- 3 G. Kumar, Z.-L. Chen, S. Jena and M. H. Huang, *J. Mater. Chem. C*, 2023, **11**, 3885–3888.
- 4 K.-C. Chien, W.-Y. Yu, J.-C. Kao, Y.-C. Lo, J.-P. Chou and M. H. Huang, *J. Mater. Chem. A*, 2024, **12**, 5429–5438.
- 5 P.-L. Hsieh, G. Naresh, Y.-S. Huang, C.-W. Tsao, Y.-J. Hsu, L.-J. Chen and M. H. Huang, *J. Phys. Chem. C*, 2019, **123**, 13664–13671.
- 6 Z.-L. Chen and M. H. Huang, *J. Mater. Chem. A*, 2023, **11**, 22198–22205.
- 7 H.-H. Ma and M. H. Huang, *J. Mater. Chem. C*, 2023, **11**, 5857–5866.
- 8 Y.-C. Yang, Y.-W. Peng, A.-T. Lee, G. Kumar and M. H. Huang, *Inorg. Chem. Front.*, 2021, **8**, 4685–4695.
- 9 P.-S. Chang, B.-H. Chen, Y.-C. Lin, W.-T. Dai, G. Kumar, Y.-G. Lin and M. H. Huang, *Small*, 2024, **20**, 2401558.
- 10 G. Kumar, H.-W. Sun and M. H. Huang, *ACS Appl. Nano Mater.*, 2024, **7**, 2155–2163.
- 11 C.-K. Chen, B.-H. Chen and M. H. Huang, *Chem. Mater.*, 2023, **35**, 7859–7866.
- 12 J.-W. Chen, A. Pal, B.-H. Chen, G. Kumar, S. Chatterjee, K. Peringeth, Z.-H. Lin and M. H. Huang, *Small*, 2023, **19**, 2205920.
- 13 Y.-J. Chuang, A. Pal, B.-H. Chen, S. Jena, S. Suresh, Z.-H. Lin and M. H. Huang, *Chem. Sci.*, 2025, **16**, 3285–3295.
- 14 B.-H. Chen, G. Kumar, Y.-J. Wei, H.-H. Ma, J.-C. Kao, P.-J. Chou, Y.-C. Chuang, I.-C. Chen, J.-P. Chou, Y.-C. Lo and M. H. Huang, *Small*, 2023, **19**, 2303491.
- 15 J. Zhuang, Q. Tian, S. Lin, W. Yang, L. Chen and P. Liu, *Appl. Catal., B*, 2014, **156–157**, 108–115.
- 16 Q. Zhang, Y. Wang, Y. Jia, W. Yan, Q. Li, J. Zhou and K. Wu, *Molecules*, 2023, **28**, 7134.
- 17 R. Ali and M. Yashima, *J. Solid State Chem.*, 2005, **178**, 2867–2872.
- 18 T. Křenek, T. Kovářik, J. Pola, T. Stich and D. Docheva, *Open Ceram.*, 2021, **8**, 100177.
- 19 M. Passi and B. Pal, *Powder Technol.*, 2021, **388**, 274–304.
- 20 H. Qiu, A. Yamamoto and H. Yoshida, *ChemCatChem*, 2024, **16**, e202301736.
- 21 T. Kimijima, K. Kanie, M. Nakaya and A. Muramatsu, *CrystEngComm*, 2014, **16**, 5591–5597.
- 22 S. Rej, M. Bisetto, A. Naldoni and P. Fornasiero, *J. Mater. Chem. A*, 2021, **9**, 5915–5951.
- 23 Z.-H. Su, M.-H. Hsieh, Z.-L. Chen, W.-T. Dai, E.-T. Wu and M. H. Huang, *Chem. Mater.*, 2023, **35**, 2782–2789.
- 24 P.-J. Chou, W.-Y. Yu, J.-C. Kao, Y.-C. Lo, J.-P. Chou and M. H. Huang, *J. Mater. Chem. A*, 2023, **11**, 19514–19523.
- 25 M.-H. Hsieh, Z.-H. Su, E.-T. Wu and M. H. Huang, *ACS Appl. Mater. Interfaces*, 2023, **15**, 11662–11669.
- 26 E.-T. Wu and M. H. Huang, *ACS Catal.*, 2023, **13**, 14746–14752.
- 27 G.-R. Wang and M. H. Huang, *J. Mater. Chem. A*, 2024, **12**, 13792–13799.
- 28 Y.-C. Chen, X.-F. Huang, H.-T. Hsu, E.-T. Wu, C.-H. Peng and M. H. Huang, *J. Mater. Chem. A*, 2024, **12**, 14792–14800.
- 29 P. Anandaraj, R. Ramesh and J. G. Malecki, *J. Organomet. Chem.*, 2023, **985**, 122577.
- 30 T. Roth, M. L. Morningstar, P. L. Boyer, S. H. Hughes, R. W. Buckheit and C. J. Michejda, *J. Med. Chem.*, 1997, **40**, 4199–4207.
- 31 P. Tamang, *Asian J. Pharm. Sci.*, 2020, **8**, 26–32.
- 32 X. Han, H. Ma and Y. Wang, *Russ. J. Org. Chem.*, 2008, **44**, 863–865.
- 33 C. Zhang, Z. Zhang and N. Jiao, *Green Chem.*, 2012, **14**, 3273–3276.
- 34 Z. Wang, T. Song and Y. Yang, *Synlett*, 2019, **30**, 319–324.
- 35 Q. Guan, Q. Sun, L. Wen, Z. Zha, Y. Yang and Z. Wang, *Org. Biomol. Chem.*, 2018, **16**, 2088–2096.
- 36 K. Sun, H. Shan, G. P. Lu, C. Cai and M. Beller, *Angew. Chem., Int. Ed.*, 2021, **60**, 25188–25202.
- 37 Z.-S. Huang, Y.-F. Wang, M.-Y. Qi, M. Conte, Z.-R. Tang and Y.-J. Xu, *Angew. Chem., Int. Ed.*, 2024, **63**, e202412707.
- 38 Y.-F. Wang, M.-Y. Qi, M. Conte, Z.-R. Tang and Y.-J. Xu, *Angew. Chem., Int. Ed.*, 2023, **62**, e202304306.
- 39 W.-K. An, S.-J. Zheng, H.-X. Zhang, H.-T. Shang, H.-R. Wang, X.-J. Xu, Q. Jin, Y. Qin, Y. Ren, S. Jiang, C.-L. Xu, M.-S. Hou and Z. Pan, *Green Chem.*, 2021, **23**, 1292–1299.



- 40 H. Pang, D. Huang, Y. Zhu, X. Zhao and Y. Xiang, *Chem. Sci.*, 2023, **14**, 1543–1550.
- 41 X. Wang, K. Huang, L. Yuan, S. Li, W. Ma, Z. Liu and S. Feng, *ACS Appl. Mater. Interfaces*, 2018, **10**, 28219–28231.
- 42 X. Yang, J. Fu, C. Jin, J. Chen, C. Liang, M. Wu and W. Zhou, *J. Am. Chem. Soc.*, 2010, **40**, 14279–14287.
- 43 M. A. Ehsan, R. Naeem, V. McKee, A. Rehman, A. S. Hakeem and M. Mazhar, *J. Mater. Sci.: Mater. Electron.*, 2018, **30**, 1411–1424.
- 44 M. J. Polking, M.-G. Han, A. Yourdkhani, V. Petkov, C. F. Kisielowski, V. V. Volkov, Y. Zhu, G. Caruntu, A. P. Alivisatos and R. Ramesh, *Nat. Mater.*, 2012, **11**, 700–709.
- 45 C. Han, J. Liu, W. Yang, Q. Wu, H. Yang and X. Xue, *J. Photochem. Photobiol. A*, 2016, **322–323**, 1–9.
- 46 Y.-H. Chiu, F.-F. M. Chang, C.-Y. Chen, M. Sone and Y.-J. Hsu, *Catalysts*, 2019, **9**, 430.
- 47 J.-Y. Ho and M. H. Huang, *J. Phys. Chem. C*, 2009, **113**, 14159–14164.
- 48 W.-C. Huang, L.-M. Lyu, Y.-C. Yang and M. H. Huang, *J. Am. Chem. Soc.*, 2012, **134**, 1261–1267.
- 49 H. Togashi, H. Shinzawa, T. Matsuo, Y. Takeda, T. Takahashi and M. Aoyama, *Free Radic. Biol. Med.*, 2000, **28**, 846–853.
- 50 M. A. Tzani, C. Gabriel and I. N. Lykakis, *Nanomater*, 2020, **10**, 2405.
- 51 A. Pal, A. Ganguly, P.-H. Wei, S. R. Barman, C.-C. Chang and Z.-H. Lin, *Adv. Sci.*, 2024, **11**, 2307266.

